

Vortex-induced vibrations: a soft coral feeding strategy?

Mouad Boudina* and Frédéric P. Gosselin

Laboratory for Multiscale Mechanics (LM2), Polytechnique Montréal, Montréal, Québec, Canada and
Department of Mechanical Engineering, Polytechnique Montréal, Montréal, Québec, Canada

Stéphane Étienne

Department of Mechanical Engineering, Polytechnique Montréal, Montréal, Québec, Canada

Soft corals, such as the bipinnate sea plume *Antillogorgia bipinnata*, are colony building animals that feed by catching food particles brought by currents. With their flexible skeleton, they bend and sway back and forth when a surface wave passes over. In addition to this low frequency sway of the whole colony, branches of *A. bipinnata* vibrate at high frequency with small amplitude and transverse to the flow as the wave flow speed peaks. We inquire into the origin of these yet unexplained vibrations and investigate their effect on soft corals. Estimation of dynamical variables along with finite element implementation of the wake-oscillator model favour vortex-induced vibrations (VIV) as the most probable origin of the observed rapid dynamics. To assess the impact of these dynamics on filter feeding, we simulated particles advected by flows around a circular cylinder and calculated the capture rate with an in-house monolithic fluid-structure interaction (FSI) finite element solver and Python code. We found that vibrating cylinders can capture up to 40% more particles than fixed ones at frequency lock-in. Thence, VIV plausibly offer soft corals better food capture.

I. INTRODUCTION

Corals thrive in nutrient poor waters, where seaweeds and seagrasses do not grow. Corals can do this in part because they benefit from the photosynthesis of their symbiotic algae zooxanthellae, but also by passively filter-feeding on food particles brought by the ambient water flow [1]. Soft corals adopt various strategies to intercept food particles. For example, the sea fans *Gorgonia ventalina* and *Gorgonia flabellum* grow with their skeleton plane perpendicular to the predominant current, hence maximising their surface area normal to the flow [2]. The bipinnate sea plume *Antillogorgia bipinnata*, in the same *Gorgoniidae* family as sea fans [3], grows to form flexible colonies with an arborescent morphology like the one represented in figure 1(a). Gosselin [4] describes a peculiar motion of *A. bipinnata*: it sways back and forth under the low frequency (~ 0.4 Hz) forcing of wave action. When the water flow speed peaks in the surface wave cycle, the branches of *A. bipinnata* undergo high frequency (~ 7 Hz) vibrations transverse to the flow. In the present paper, we show how vortex-induced vibrations are responsible for the high frequency vibration of *A. bipinnata*, and how these dynamics increase the food particle capture efficiency, as schematised in figure 1.

To cope with the ambient fluid flows, arborescent species, on land or underwater, rely chiefly on their flexibility. In presence of a steady current, they are known to streamline and reconfigure their shape in order to minimise the hydrodynamic drag and prevent breakage [4–6]. This incentive is amongst the reasons why soft corals, along with other species, modulate the length and stiffness of their branches [7, 8]. Under oscillatory flow, such as wave surge, their stems sway back and forth periodically and exhibit specific deformation profiles depending on the wave frequency and water speed [9, 10]. As for the interaction of the flow with structures having a branching pattern, the response is a complex motion involving series of vibrational modes with frequencies close to each other [11–13]. *A. bipinnata* exhibits all these behaviours: its main stem reconfigures and sways with the wave surges, and its branches vibrate rapidly spanning small transverse amplitudes.

Vortex-induced vibrations (VIV) are common in marine environment, leading to small and rapid oscillations [14–16]. In the case of a spring-mounted circular cylinder, they can appear for Reynolds numbers as low as 20 [17], and become pronounced when the von Kármán vortex street establishes in the wake. As the frequency of vortex shedding gets close to the natural frequency of the spring-mounted cylinder, the structure and the wake dynamics synchronise and amplify. This state is known as frequency synchronisation or *lock-in* [18]. Flexible structures may exhibit several frequency lock-in ranges due to the multiplicity of their natural frequencies [19]. VIV along flexible structures propagate either as travelling waves when the structure has free endpoints [20, 21], standing waves when it has pinned endpoints [22], or a mix of both modes when the flow is non-uniform [23, 24]. In the living world, vortices

* Electronic mail: mouad.boudina@polymtl.ca

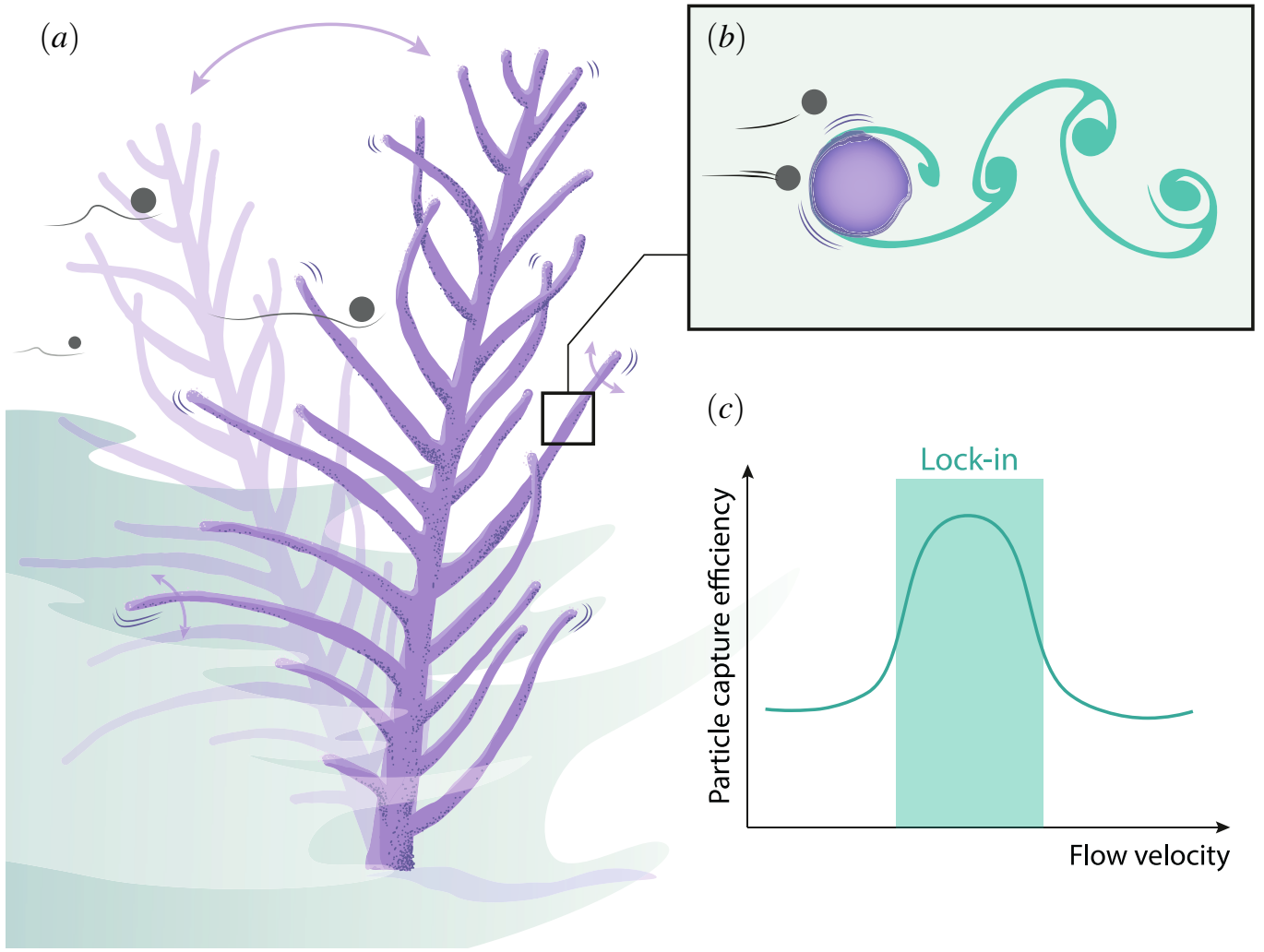


FIG. 1. (a) Schematic of a bipinnate sea plume *A. bipinnata* swaying back and forth under the surface wave action, with branches exhibiting small and rapid transverse vibrations. It stands perpendicular to the flow and encounters the incoming food particles. (b) Cross-section of a branch vibrating due to the vortex shedding in the wake, and facing two incoming particles. The upper particle crosses over the branch and escapes capture, whereas the lower one approaches the branch surface and gets intercepted. (c) Schematic summary of the numerical results of the particle capture efficiency, as defined in equation (1), versus flow speed. The soft coral branch maximises the efficiency of particle capture during the lock-in phase, where the vortex shedding frequency synchronises with the natural frequency of the branch. Art by © IMPAKT Scientifik.

have been credited as a potential factor in biological processes such as spore dispersal on plants [25] and edible particle filtering for black fly and mosquito larvae in water. Chance and Craig [26] and Widahl [27] suggested qualitatively that, being suspended in water, these larvae create vortices as a strategy to drive more food up to their fans. By increasing the food particle capture rate, we believe that VIV might be a boon to soft corals.

Soft corals are colonies of polyps, which are small tubular organisms with tentacles, mouth, and digestive system [28, 29]. They are passive filter feeders [1], waiting passively for water currents to carry its particulate nutritional content (e.g. detritus, organic debris, phytoplankton, protists). When an edible particle comes close to a polyp, the tentacles stretch and catch it (encounter phase), then retain it by activating spines or secreting mucus (retention phase) [30]. The study of particle capture is important to evaluate the filtering efficiency of such species and connect it with the flow properties. In particle filtering literature, especially in the field of fluid mechanics and chemistry, encounter and retention are combined into a single phase termed ‘capture’ or ‘interception’. Multiple studies have considered the particle capture of a circular cylinder [31–35]. Weber and Paddock [31] and Palmer *et al.* [32] defined the capture efficiency as

$$\eta = \frac{\dot{N}}{\dot{N}_{\text{init}}}, \quad (1)$$

where \dot{N} is the rate of captured particles and \dot{N}_{init} is the rate of released particles, and found that it increases with the cylinder-based Reynolds number and the particle size, as well as the surface roughness. Surprisingly, data on particle capture by vibrating collectors are scarce. Even the handful of papers that examined the effect of collector motion [36, 37] were imposing oscillation frequencies and amplitudes, not always covering the vibration parameter range seen in the living world. Field experiments on a timothy grass revealed that it captured and germinated more pollen than transverse-tethered and stream-wise-tethered ones [37]. This example indicates that it is important to let the collector free to move instead of imposing oscillations. Not only the motion is more realistic, but the vibration amplitude and frequency vary simultaneously with the flow and cylinder parameters and cannot be decoupled. Although the idea that vibrations could improve particle capture was already suspected [38], there are no explicit mention of VIV in the particle interception literature, and the variation of the capture efficiency with the relevant dynamical parameters remains unclear due to absence of quantitative data.

Understanding more about corals is critical as they form the basis of ecosystems home to countless fish and invertebrates. These coral reef ecosystems are under the multi-pronged threat of global warming: ocean acidification, water temperature rise, and more frequent hurricane passage. All coral species are not affected the same by these threats, soft coral species seeming to fare better in these changing environmental conditions [39, 40]. The existing hydrodynamic studies of corals, are mostly limited to the hard reef-building kind [41]. The biological role of soft coral flexibility in their fluid-structure interaction remains relatively unexplored.

This paper intends to fill this gap and prove that VIV can increase the capture rate of a cylindrical branch. For this aim, we divide the ensuing work into two parts. We first present qualitative and quantitative arguments that put forward vortex-induced vibrations as the most probable source of the fast motion of soft coral branches. In the second part, we model the branch as a circular cylinder free to oscillate in transverse and stream-wise directions, and compute its interaction with fluid flows using two-dimensional direct numerical simulations (DNS). We integrate the trajectories of particles advected by the flow, calculate the rate of capture, and compare it with the case of a fixed cylinder. Finally, using results of the capture rate, we propose to draw a link between the morphology of soft corals and the predominant local water speeds.

II. ORIGIN OF VIBRATIONS

Gosselin [4] reports a vibrating bipinnate sea plume *A. bipinnata* on a SCUBA dive off of Isla Mujeres near Cancun, Mexico on March 25th 2015, at about 10m depth. The vibrational dynamics are similar to those seen in an online recorded video [42]. Using the software IMAGEJ [43], we assessed from that video that the flow velocity was $U_0 \sim 10$ cm/s and the wave period $T_{\text{wave}} \sim 5$ s. With a branch diameter of $D \sim 2$ mm [44, 45], and given the water kinematic viscosity $\nu_f \sim 10^{-6}$ m²/s, the Reynolds number and the Keulegan-Carpenter number in the stream-wise direction are $Re = U_0 D / \nu_f \sim 200$ and $KC = U_0 T_{\text{wave}} / D \sim 250$, meaning that the flow is under vortex shedding regime [16]. Finally, from an estimated value of the vibration frequency of $f_n \sim 7 - 9$ Hz, the reduced velocity is $U_r = U_0 / f_n D \sim 5 - 7$, which suggests a VIV lock-in dynamics.

As far as VIV might be in play, we sought to reproduce the observed coral branch motion by simulating its reconfiguration and vibration under flow. For this, we used RodiCS [46], a finite element solver of Kirchhoff rods based on the FEniCS platform [47]. The dynamics of a branch is modelled with rod elements which consider the dynamical three-dimensional bending and torsion for arbitrarily large deformation. This deformation is due to a static drag force based on the semi-empirical formulation of [48] and a dynamical coupling with the shed vortices, which are accounted in the wake-oscillator model of Facchinetti *et al.* [49]. Details on the Kirchhoff equations, the wake-oscillator model, as well as the verification and validation of RodiCS [46], are provided in the Other Supplementary Information. We take again a representative diameter of $D \sim 2$ mm. We focused on branches having lengths of $L \sim 1, 5$, and 8 cm. Moreover, we considered a coral density equal to the fluid density $\rho_s \sim \rho_f \approx 10^3$ kg/m³. This choice is realistic because soft coral branches are not floating up or falling down, so they can be considered as approximately neutrally-buoyant. As for the flexural rigidity, we conducted three-point bending tests on wet soft coral branches freshly taken out from aquarium. We found a flexural rigidity of order $EI \sim 5 \times 10^{-7}$ N.m². We simulated a water flow of speed $U_0 \sim 10$ cm/s, as estimated above from the online video.

Numerical deformation profiles are shown in figure 2. A first common feature in simulations and real coral observations is the extent of bending in the water flow direction. Both the elastic rod and branches of $L \sim 1$ cm remain relatively straight, whereas the ones with $L \sim 5$ and 8 cm reconfigure more with the flow. A second common feature is the transverse envelope of vibrations. Short branches and rods exhibit a first modal shape with a maximum deflection at the tip, whereas longer ones have a second modal shape with a single zero-displacement node. These similarities between the simulations and the video observations are additional clues supporting our hypothesis that VIV are the most probable origin of the observed rapid motion of soft coral branches.

Furthermore, we show that other types of flow-induced vibrations cannot be the principal cause of the sustained

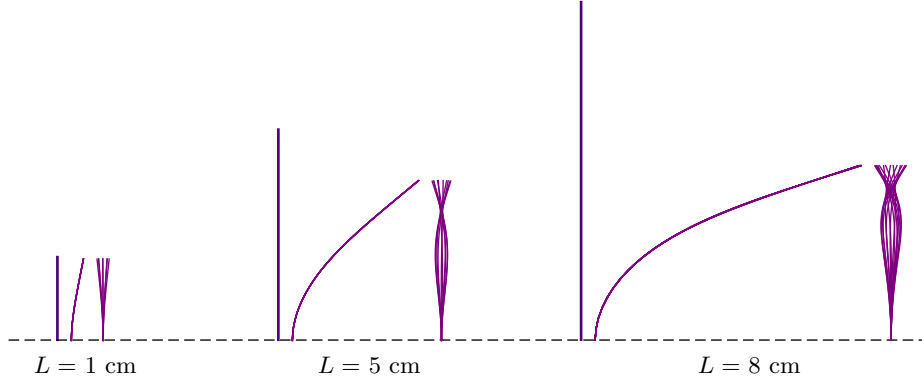


FIG. 2. Numerical deformation profiles of elastic rods of lengths $L = 1$, 5 and 8 cm subjected to VIV in a unidirectional flow. The vertical line in the left of each case indicates the initial configuration of the rod. On the middle and the right are the lateral and frontal profiles. The lengths are proportional. In the online record of the vibrating soft coral, we also see small branches staying relatively straight and having a first mode vibration, and longer branches reconfiguring more with the flow and having a second mode vibration with a single zero-displacement node.



FIG. 3. Dried bipinnate sea plume *Antillogorgia bipinnata* (Nova South Eastern University [53], © Charles G. Messing). The centre-to-centre separation space between branches goes from 4.5 to 8.5 diameters. The cortex of some polyps can be discerned in the extremities of the branches (top left, bottom left, and bottom right of the image).

soft coral vibration. If the vibration was induced by an external excitation, such as turbulent buffeting, the branch frequency would match the peak frequency f_{peak} of the sea wave spectrum in the region. From the National Data Buoy Center website [50], the peak frequencies of shallow-waters in the Gulf of Mexico, where some soft corals live, ranged from 0.15 to 0.24 Hz, which is $f_n/f_{\text{peak}} \sim 40$ times slower than the branch motion. If the flow stream was to buffet the coral, it might induce the back and forth gentle sway of the entire coral, but not the rapid dynamics of the branches.

Additionally, even though the coral branches lay side-by-side in the same plane facing the flow, we do not suspect a fluidelastic instability to take place. In fact, if a pair of cylinders are separated by a centre-to-centre distance less than ~ 4 diameters, they generate either a combined, a bistable asymmetric, or a coupled vortex shedding, which triggers vibrations [51, 52]. We based our estimation on the dried *A. bipinnata* pictured in figure 3, and found that the separation distance was between 4.5 diameters and 8.5 diameters. Therefore, the branches are fairly isolated from each other to shed independent vortex streets and prevent any fluidelastic instability.

A final plausible cause of vibration that might be involved is galloping. A branch cross-section is overall circular. It is known that circular cylinders are ‘immune to galloping’ and undergo only VIV [54, 55]. Though, one might

think that the coral branch is not perfectly circular due to the polyps covering it. Assuming they represent small geometrical perturbations, we simulated flows around an idealised cross-section of a soft coral branch of *A. bipinnata* using an in-house flow solver [56], as detailed in appendix A. We found that the Glauert-den Hartog criterion was unfulfilled, implying that galloping is implausible as the source of soft coral branch vibrations.

In summary, turbulent buffeting, fluidelastic instability, and galloping cannot be the source of the high frequency vibration of *A. bipinnata* branches, which bear all the telltale signs of VIV.

III. PARTICLE ADVECTION

A. Coral branch as a spring-mounted circular cylinder in flow

Following the identification of VIV as the source of soft coral branch vibration, we model the capture of particles advected by the fluid flow. We first idealise the coral branch as a circular cylinder. From a geometrical perspective, the polyps covering the branch of *A. bipinnata* are small perturbations, of about 10% of the branch diameter [44]. From a fluid-structure interaction perspective, isolated circular cylinders are only prone to VIV [54], which is the flow-induced vibration we are interested in. Additionally, simplifying the coral branch to a circular cylinder brings our study back into the classical problem of particle capture by a circular collector in the field of particle filtering.

We simulate a fluid flow of upstream velocity U_0 around a fixed or vibrating cylinder of diameter D , in order to highlight the effect of vibration on particle capture. We consider the water flow incompressible and two-dimensional. In addition, we assume it is unidirectional because the Keulegan-Carpenter number in the stream-wise direction is sufficiently large $KC \sim 250$, as estimated in section II, and we are interested in the vortex shedding regime. The flow is governed by the continuity and Navier-Stokes equations, written in an Arbitrary Lagrangian Eulerian (ALE) framework

$$\nabla \cdot \mathbf{U}_f = 0, \quad (2a)$$

$$\frac{\partial \mathbf{U}_f}{\partial t} + [(\mathbf{U}_f - \mathbf{V}) \cdot \nabla] \mathbf{U}_f = \frac{1}{\rho_f} [-\nabla p + \mu_f \nabla^2 \mathbf{U}_f], \quad (2b)$$

where ρ_f , μ_f , \mathbf{U}_f , and p are respectively the fluid density, dynamic viscosity, velocity, and pressure. The vector \mathbf{V} is the velocity of the moving mesh. If the cylinder is fixed, we simply have $\mathbf{V} = \mathbf{0}$. The hydrodynamic load applied on the cylinder is expressed as

$$\mathbf{F}_{\text{hydro}} = \oint [-p\mathbf{I} + \mu_f (\nabla \mathbf{U}_f + \nabla \mathbf{U}_f^T)] d\mathbf{n}, \quad (3)$$

with $d\mathbf{n}$ being the integration element around the cylinder, pointing outwards. Besides, we consider the cylinder as a spring-mounted oscillator free to move stream-wise and transverse to the main flow under the hydrodynamic load $\mathbf{F}_{\text{hydro}}$, as schematised in figure 4(a). Neglecting structural damping, the position of the cylinder centre \mathbf{X}_{cyl} is solution of

$$m \frac{d^2 \mathbf{X}_{\text{cyl}}}{dt^2} + k \mathbf{X}_{\text{cyl}} = \mathbf{F}_{\text{hydro}}. \quad (4)$$

where $m = \pi \rho_s D^2/4$ is the cylinder mass and k the spring stiffness, both per unit length.

Normalising velocities with U_0 and distances with D , and scaling time by D/U_0 and pressure by $\rho_f U_0^2$, the governing equations of the fluid and cylinder interaction can be rewritten as

$$\bar{\nabla} \cdot \bar{\mathbf{U}}_f = 0, \quad (5a)$$

$$\frac{\partial \bar{\mathbf{U}}_f}{\partial \bar{t}} + [(\bar{\mathbf{U}}_f - \bar{\mathbf{V}}) \cdot \bar{\nabla}] \bar{\mathbf{U}}_f = \left[-\bar{\nabla} \bar{p} + \frac{1}{Re} \bar{\nabla}^2 \bar{\mathbf{U}}_f \right], \quad (5b)$$

$$\bar{\mathbf{F}}_{\text{hydro}} = \oint \left[-\bar{p}\mathbf{I} + \frac{1}{Re} (\bar{\nabla} \bar{\mathbf{U}}_f + \bar{\nabla} \bar{\mathbf{U}}_f^T) \right] d\bar{\mathbf{n}}, \quad (5c)$$

$$\frac{d^2 \bar{\mathbf{X}}_{\text{cyl}}}{d\bar{t}^2} + \left(\frac{2\pi}{U_r} \right)^2 \bar{\mathbf{X}}_{\text{cyl}} = \frac{4/\pi}{M} \bar{\mathbf{F}}_{\text{hydro}}, \quad (5d)$$

with the bar ($\bar{\cdot}$) denoting dimensionless variables. The dynamical parameters present in the system of equations (5) are the Reynolds number Re , the reduced velocity U_r , and the mass number M defined as

$$Re = \frac{\rho_f U_0 D}{\mu_f}, \quad U_r = \frac{2\pi U_0}{D} \sqrt{\frac{m}{k}}, \quad M = \frac{m}{\pi \rho_f D^2/4}. \quad (6)$$

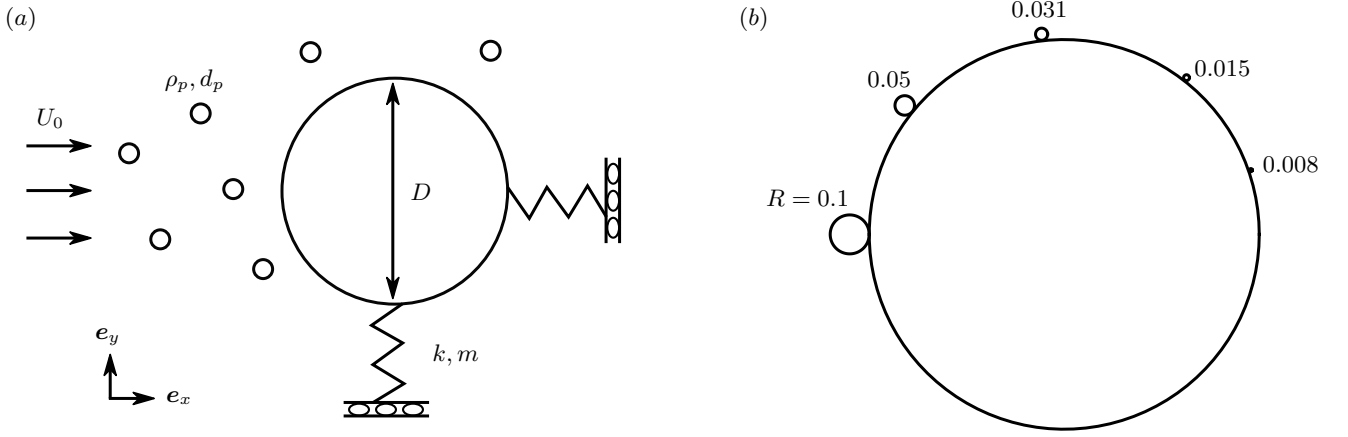


FIG. 4. (a) Schematics of particles advected by a flow around a cylinder free to oscillate in the transverse and stream-wise directions. The upstream fluid velocity is parallel to e_x . Particles have a density ρ_p and diameter d_p . The mass per unit length of the cylinder is m , and the spring stiffness per unit length k is the same in both directions. (b) Drawing contrasting the size of particles simulated with the size of the cylinder, with $R = d_p/D$ being the diameter ratio.

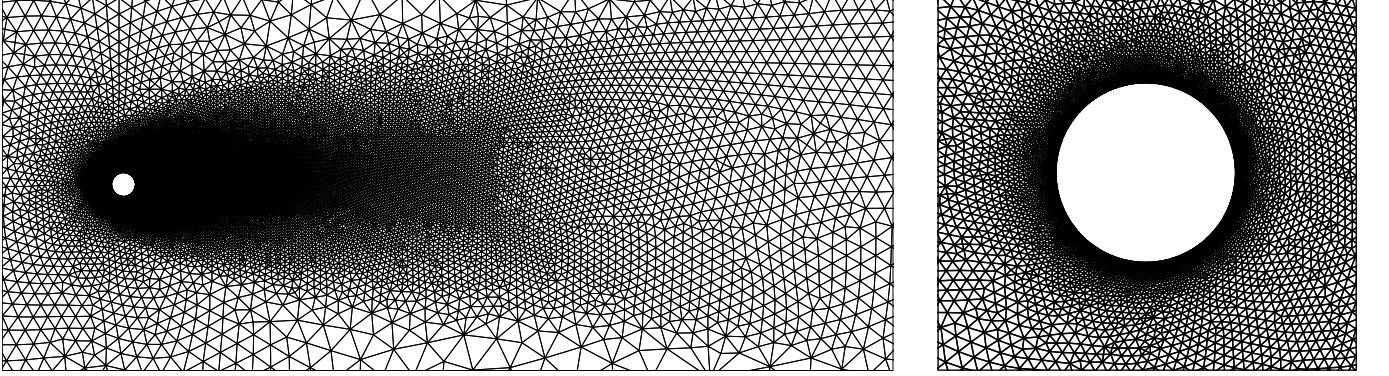


FIG. 5. Close-ups of the fluid mesh highlighting the densification in the wake (left) and around the boundary layer (right).

As mentioned in section II, we suppose that soft coral branches have a density roughly the same as water $\rho_s \sim \rho_f$, thus we consider a constant cylinder mass number $M = 1$ throughout this study.

Figure 5 shows the computational domain. The dimensions are large enough ($-40 \leq \bar{x} \leq 120$ and $-60 \leq \bar{y} \leq 60$) to avoid confinement effects [57]. The domain is discretised with 96 000 nodes and 48 000 Taylor-Hood ($\mathcal{P}_2 - \mathcal{P}_1$) triangular elements [58], it follows that the velocity is third order accurate and the pressure is second order accurate. These elements are small in the wake and close to the cylinder to resolve the vortex shedding and the boundary layer. The grid in figure 5 was validated in Etienne and Pelletier [17] and yielded accurate results in good agreement with existing data. The boundary conditions on the fluid velocity \bar{U}_f are a uniform Dirichlet at the entry ($\bar{x} = -40$), homogeneous Neumann at the exit ($\bar{x} = 120$), symmetry at the top and bottom boundaries ($\bar{y} = \pm 60$), and no-slip at the cylinder wall.

B. Particle dynamics

Regarding food particles, we consider them as spheres of diameter d_p and density ρ_p . Several governing equations were established to describe the motion of particles in non-uniform or random flow fields [59–61]. They included terms displaying the influence of particles on the flow. However, in the present study we assume that the particles do not disturb the flow and cannot change actively their trajectory, unlike a swimming plankton for instance. Then the suitable governing equation to consider is the Basset-Boussinesq-Oseen (BBO) equation [61, 62]. We neglect gravity effects, and the remaining forces applied on a particle that we keep are the drag \mathbf{F}_D , the pressure load \mathbf{F}_P , and the

added mass force \mathbf{F}_A . The governing equations describing the particle trajectory are

$$\frac{d\mathbf{x}_p}{dt} = \mathbf{u}_p, \quad (7a)$$

$$\frac{d\mathbf{u}_p}{dt} = \frac{1}{m_p}(\mathbf{F}_D + \mathbf{F}_P + \mathbf{F}_A), \quad (7b)$$

where $m_p = \rho_p \pi d_p^3 / 6$ is the mass of the particle, \mathbf{x}_p its position, and \mathbf{u}_p its velocity.

The drag applied on a sphere reads

$$\mathbf{F}_D = -\frac{1}{2} C_D^{\text{sph}} \rho_f \pi \left(\frac{d_p}{2} \right)^2 \|\mathbf{u}_p - \mathbf{U}_f\| (\mathbf{u}_p - \mathbf{U}_f). \quad (8)$$

which is the same expression if the flow were steady. Here C_D^{sph} is the drag coefficient of a sphere, it is a function of the particle-based Reynolds number

$$Re_p = \frac{\rho_f \|\mathbf{u}_p - \mathbf{U}_f\| d_p}{\mu_f}. \quad (9)$$

Because this latter is unknown *a priori*, we considered the Schiller-Nauman interpolation [62]

$$C_D^{\text{sph}} = \frac{24}{Re_p} (1 + Re_p^{0.687}), \quad (10)$$

which is valid for $Re_p < 800$. Second, the pressure load is related to the pressure gradient through

$$\mathbf{F}_P = -\frac{4}{3} \pi \left(\frac{d_p}{2} \right)^3 \nabla p. \quad (11)$$

It is also known as the Froude-Krylov force [16] due to the difference in pressure of the global flow, which depicts the unsteadiness of the flow in absence of the particle. If the fluid were stagnant, there would be no pressure gradient accelerating it and this force would simply vanish.

Finally, although previous studies ignored the added mass force [33, 36], we deem important to include it in the force balance. It is proportional to the particle acceleration relative to the fluid

$$\mathbf{F}_A = -C_m \rho_f \frac{4}{3} \pi \left(\frac{d_p}{2} \right)^3 \left(\frac{d\mathbf{u}_p}{dt} - \frac{d\mathbf{U}_f}{dt} \right). \quad (12)$$

Here C_m is the mass coefficient of a sphere. We took it as constant equal to 1/2. Generally, it increases rapidly when the particle comes close to the wall [63], so our leading order simplification becomes invalid in proximity of the cylinder. An elaborate model would account not only for a varying mass coefficient, but also for the repulsive effect just prior to capture due to confinement, for example by including an additional force in the momentum equation (7) [64]. In our entire simulations, however, we keep the assumption $C_m = 1/2$.

Denoting the ratio of diameters

$$R = \frac{d_p}{D}, \quad (13)$$

the particle-based Reynolds number reads $Re_p = Re R \|\bar{\mathbf{u}}_p - \bar{\mathbf{U}}_f\|$, and equations (7) become

$$\frac{d\bar{\mathbf{x}}_p}{dt} = \bar{\mathbf{u}}_p, \quad (14a)$$

$$\frac{d\bar{\mathbf{u}}_p}{dt} = \bar{\mathbf{F}}_D + \bar{\mathbf{F}}_P + \bar{\mathbf{F}}_A, \quad (14b)$$

with

$$\bar{\mathbf{F}}_D = -\frac{18}{\bar{\rho} R^2 Re} (1 + Re_p^{0.687}) (\bar{\mathbf{u}}_p - \bar{\mathbf{U}}_f), \quad (15a)$$

$$\bar{\mathbf{F}}_P = -\frac{1}{\bar{\rho}} \bar{\nabla} \bar{p}, \quad (15b)$$

$$\bar{\mathbf{F}}_A = -\frac{C_m}{\bar{\rho}} \left(\frac{d\bar{\mathbf{u}}_p}{dt} - \frac{d\bar{\mathbf{U}}_f}{dt} \right), \quad (15c)$$

where $\bar{\rho} = \rho_p/\rho_f$ is the ratio of densities. In this paper $\bar{\rho} = 2$, which we consider as an upper bound of densities of existing food particles. According to Espinosa-Gayosso *et al.* [65], a sediment-type particle 2.6 times heavier than water achieves a capture efficiency equal to that of a perfect fluid tracer if the Stokes number $Stk = \bar{\rho}R^2Re/9$ is less than 0.1 at $Re \sim 100$. For a typical simulation case at this Reynolds number we have $Stk \sim 0.06$ (e.g. taking $R \sim 0.05$), therefore the choice $\bar{\rho} = 2$ is legitimate.

C. Numerical solving

We solve the particle advection problem in two stages. First, we compute the FSI problem in an ALE framework using the in-house solver CADYF [56]. This code was verified with the method of manufactured solutions [66, 67] and for classical FSI problems such as airfoil plunging and pitching and flexible strip at the rear of a square cylinder [68]. The code is also validated and produces dynamical results consistent with data in the literature for several flow-induced vibrations including VIV of circular [17] and square [69] cylinders, and wake-induced vibrations of cylinders in tandem [70].

Initially, the fluid is at rest, $\bar{\mathbf{U}}_f = \mathbf{0}$ and $\bar{p} = 0$, and ramps up to unity $\bar{\mathbf{U}}_f = \mathbf{e}_x$ in few time steps to satisfy a divergence-free flow field. Also at initial time, the cylinder stands at the position $\bar{\mathbf{X}}_{\text{cyl}} = \mathbf{0}$. CADYF integrates the coupled system of equations (5) using hp-adaptive Backward Differential Formulas (BDF) methods [71]. The order and time step adjust automatically so that the local truncation error remains smaller than a constant absolute tolerance equal to 10^{-5} . We extract the flow solution at each instant $\bar{t}_n = n/10$ starting from $\bar{t} = 400$, long after VIV have reached their periodic limit-cycle.

Next, we export these data into PARADVECT [72], a Python code we wrote in order to integrate the system of equations (14) in a Lagrangian framework using a forward Euler scheme. A code verification of PARADVECT is available in the Other Supplementary Material. To satisfy stability, the integration time step $\Delta\bar{t}$ should be smaller than the characteristic time involved in the system $\tau = (\bar{\rho} + C_m)R^2Re/9$. We compare τ with the time step $\bar{t}_{n+1} - \bar{t}_n = 1/10$ by which we extracted the flow solution from CADYF: if $\tau > 1/10$, which is the case for large particles, we take $\Delta\bar{t} = 1/10$, whereas if $\tau < 1/10$, which is the case for small particles, we interpolate linearly the flow solution in time. Linear interpolation is appropriate because the flow solution varies smoothly during a time step of $\sim 1/10$ and does not fluctuate over the small timescale τ .

Figure 4(b) juxtaposes the cylinder and the considered particles to give an idea on their relative size. The trajectory of every particle is integrated from a unique starting line $\bar{x}_0 = 2$ upstream from the cylinder for several ordinates \bar{y}_0 . The flow in these positions is horizontal enough and unperturbed. The local fluid velocity is then assigned as their initial velocity.

To calculate the total hydrodynamic force applied on the particle, we interpolate quadratically the fluid velocity and linearly the pressure at the particle centre. As this calculation requires the knowledge of the finite element hosting the particle, we adopted the particle tracer algorithm proposed by Löhner and Ambrosiano [73]. It searches recursively, neighbour to neighbour, the new host element in the vicinity of the known previous one. This tracking technique is suitable, time-saving, and easy to implement in particle-in-cell codes, such as ours, where physical particles do not jump over many elements in a single time step [74].

Finally, we assume that the particle is captured as soon as it hits the edge of the cylinder. Since particles are spherical and the cylinder is circular, the capture occurs when $\|\bar{\mathbf{x}}_p - \bar{\mathbf{X}}_{\text{cyl}}\| \leq (1 + R)/2$. We refer to this capture condition as the *solid contact* criterion.

IV. CAPTURE RATE

A. Definition

To assess the filtering ability of the cylinder, we calculate the rate by which it intercepts the particles. We define the capture rate \dot{N} as the number of particles that the cylinder captures per unit time. As represented in figure 6, the particle that would be ultimately captured enter necessarily through an opening that we call the *capture window*. Thereby, the capture rate also equals the flux of particles through this capture window

$$\dot{N} = C_0 U_0 w. \quad (16)$$

Here C_0 is the particle concentration per unit length, which we assume constant and uniform, and w is the size of the capture window.

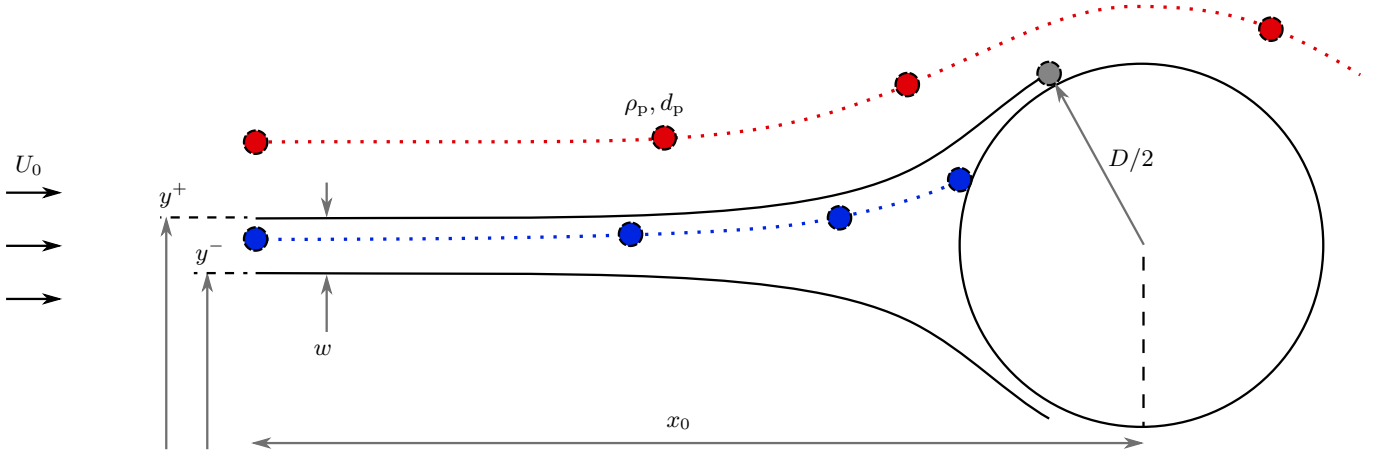


FIG. 6. Schematics of particle interception by a fixed cylinder. Particles are launched from a distance x_0 upstream from the the cylinder. Because it starts near the symmetry line, the blue particle is captured, whereas the red particle starts from a higher y -position and succeeds in crossing over the cylinder and escaping capture. The gray particle is the farthest particle that the cylinder intercepts. Its trajectory starts from the ordinate y^+ , and defines the upper border of the capture domain. The size of the capture window is $w = y^+ - y^-$.

B. Calculation strategy

1. Automated dichotomy

Owing to the definition (16), we determine the capture rate through the calculation of the size of the capture window. The upper and lower boundaries of the capture region are the trajectories of the farthest captured particles, as shown in figure 6. Thus, it suffices to calculate the ordinate of these border particles, denoted y^+ and y^- , since

$$w = y^+ - y^-. \quad (17)$$

First, we consider captured (blue) and non-captured (red) particles, launched from the same starting line x_0 upstream from the cylinder. Their initial positions, y^c and y^{nc} , are necessarily bounds of either border, say the upper one ($y^c < y^+ < y^{nc}$). Next, we release a third particle between the two previous ones, from the middle of their initial ordinates $y^m = (y^c + y^{nc})/2$. If it escapes capture, then the upper border y^+ is necessarily between the initial ordinates of this new particle and the former captured one ($y^c < y^+ < y^m$). The code PARADVECT [72] repeats this dichotomic process until it reaches a resolution of one thousandth of the particle diameter $|y^c - y^m| < d_p/1000$.

2. Temporal decomposition

When the cylinder vibrates, the borders of the capture region vary in time $y^\pm = y^\pm(t)$, and the capture strip is no longer straight, as seen in figure 7. The particles spread at time t that are captured are launched between $y^+(t)$ and $y^-(t)$. The instantaneous capture window $w(t) = y^+(t) - y^-(t)$ must be periodic, thus we propose the following ansatz

$$w(t) = \langle w \rangle + w_a \sin\left(\frac{2\pi t}{T} + \varphi\right). \quad (18)$$

The period T is not equal to the vibration period, but half of it. Indeed, as illustrated in figure 7, the cylinder describes a lemniscate, so it captures particles in the same way whether during the upper or the lower loop. In other words, the capture rate is determined by the stream-wise – not transverse – oscillations, which complete a cycle in half a period.

We should mention that the dependency on time is also true for the fixed cylinder, yet the variation of $w(t)$ is due to the periodic vortex shedding, which affects the streamlines in the front, and the period T in the ansatz (18) is equal to the vortex shedding period.

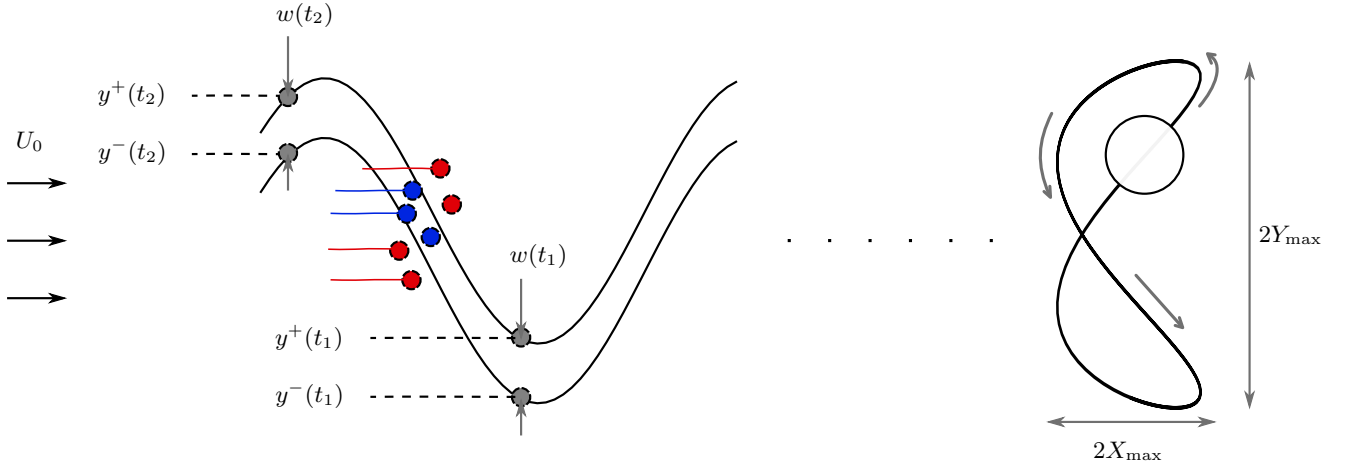


FIG. 7. Distortion of the capture domain due to vibration. The initial ordinates of the gray border particles are now varying in time $y^\pm = y^\pm(t)$. The instantaneous capture window, through which the particles launched at time t would be captured, is $w(t) = y^+(t) - y^-(t)$. At instants t between t_1 and $t_2 > t_1$, the blue particles are launched between $y^-(t)$ and $y^+(t)$, so they are captured. The red particles are launched outside these limits, so they escape capture. A portion of particle trajectories is shown in solid line. The cylinder draws a lemniscate trajectory, and Y_{\max} and X_{\max} are the transverse and stream-wise amplitudes of vibration. The motion of the cylinder is symmetric with respect to the horizontal line passing through the node of the lemniscate, hence the capture is periodic and goes in harmony with the stream-wise oscillations, which complete a cycle in half a period.

We calculate the size of the capture window at instants $t = 0, T/4$, and $T/2$, and determine the mean and fluctuating components $\langle w \rangle$ and w_a in equation (18) from the ensuing formulæ

$$\langle w \rangle = \frac{w(0) + w(T/2)}{2}, \quad (19a)$$

$$w_a = \sqrt{[w(0) - \langle w \rangle]^2 + [w(T/4) - \langle w \rangle]^2}. \quad (19b)$$

C. Dimensional analysis

The capture rate is a function of the fluid, cylinder, and particle properties

$$\begin{aligned} \dot{N} [\text{s}^{-1}], \quad U_0 [\text{m s}^{-1}], \quad \rho_f [\text{kg m}^{-3}], \quad \mu_f [\text{kg m}^{-1}\text{s}^{-1}], \quad D [\text{m}], \quad k [\text{N m}^{-2}], \\ m [\text{kg m}^{-1}], \quad d_p [\text{m}], \quad \rho_p [\text{kg m}^{-3}], \quad C_0 [\text{m}^{-2}]. \end{aligned} \quad (20)$$

For convenience, we discard the variation in time t owing to the decomposition in equation (18). The Buckingham Π theorem [75] states, hence, that a relation exists between $10 - 3 = 7$ independent dimensionless variables, that we choose to be

$$\begin{aligned} \eta = \frac{\dot{N}}{C_0 U_0 D}, \quad Re = \frac{\rho_f U_0 D}{\mu_f}, \quad R = \frac{d_p}{D}, \quad U_r = \frac{2\pi U_0}{D} \sqrt{\frac{m}{k}}, \\ \bar{\rho} = \frac{\rho_p}{\rho_f}, \quad M = \frac{m}{\rho_f D^2}, \quad \bar{C}_0 = C_0 D^2. \end{aligned} \quad (21)$$

In this way, the dimensionless capture rate η is also the capture efficiency defined by Weber and Paddock [31], Palmer *et al.* [32], Espinosa-Gayosso *et al.* [34, 35], which itself, from the definition (16), equals the dimensionless size of the capture window

$$\eta = \frac{\dot{N}}{C_0 U_0 D} = \frac{w}{D} = \bar{w}. \quad (22)$$

According to equation (18), it follows that

$$\eta = \langle \eta \rangle + \eta_a \sin\left(\frac{2\pi t}{T} + \varphi\right), \quad (23)$$

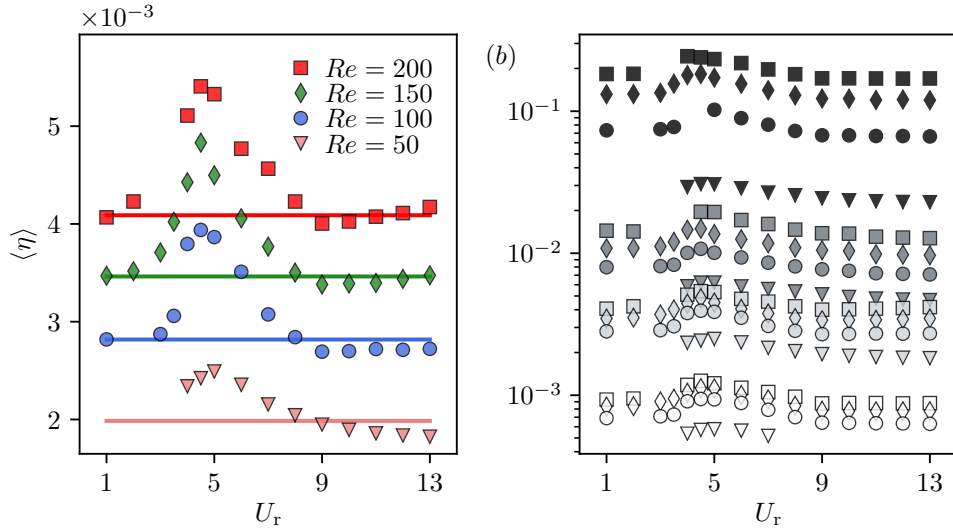


FIG. 8. Mean capture rate $\langle \eta \rangle$ versus the reduced velocity for (a) the particle of diameter ratio $R = 0.031$, and for (b) all particles $0.015 \leq R \leq 0.1$ in flows of Reynolds numbers $50 \leq Re \leq 200$. In (b), the y -axis is logarithmic, and each group of four curves with a single gray level corresponds to the particles $R = 0.015$ (white), 0.031 (light gray), 0.05 (dim gray), and 0.1 (black).

with $\langle \eta \rangle = \langle w \rangle / D$ and $\eta_a = w_a / D$. For all simulations in the present work, we kept a constant and uniform particle concentration $\bar{C}_0 = \text{const.}$ In addition, as we assumed in section III, we choose $M = 1$ and $\bar{\rho} = 2$. Henceforth, the remaining variables that determine the capture rate are the Reynolds number Re , the diameter ratio R , and the reduced velocity U_r .

V. RESULTS

To see how the vibration affects the capture rate, we let the cylinder free to oscillate, and varied the spring stiffness so that the reduced velocities were between $U_r = 1$ and 13 , covering the estimation made in section II. We simulated the trajectories of particles having diameter ratios $0.015 \leq R \leq 0.1$ as for phytoplankton and larvae [76]. The flows considered have Reynolds numbers ranging from $Re = 50$ to 200 , which are the limits, respectively, of the establishment of the laminar von Kármán vortex street and the transition into three-dimensional vortex shedding.

In equation (23), we found a ratio $\eta_a / \langle \eta \rangle_{\text{fixed}}$ less than 2% for the fixed case, meaning that the temporal term can be regarded as a small fluctuation. For the vibrating case this ratio was larger $\eta_a / \langle \eta \rangle \lesssim 20\%$. We did not investigate the time fluctuations of particle capture rate, we instead focused on the time-averaged capture rate since it is most relevant in terms of filtering applications and biological implications.

Figure 8 shows the variation of the mean capture rate $\langle \eta \rangle$ with the reduced velocity U_r . We see that $\langle \eta \rangle$ is a bell-shaped function, which starts from almost the same value as for a fixed cylinder ($U_r \sim 1$), peaks at lock-in ($U_r \sim 5$), then decreases down to values either around or less than the capture rate by a fixed cylinder. We observe in figure 8(a) that $\langle \eta \rangle$ increases with the Reynolds number Re , and from figure 8(b) it increases with the particle size R as well. The variation of the mean capture rate with these two parameters, for a given reduced velocity U_r , is shown in figure 9. We find that the mean capture rate follows the same scaling as in the fixed cylinder case $\langle \eta \rangle \sim \langle \eta \rangle_{\text{fixed}} \sim R^2 Re^{1/2}$. The square root in the Reynolds number is reminiscent of the boundary layer thickness in the cylinder wall. The boundary layer plays indeed a key role in the capture process [33], and it was the origin of the theoretical derivation and physical explanation of the power law $R^2 Re^{1/2}$ proposed by Boudina *et al.* [77].

To evaluate the benefit that vibrations bring to particle interception, we define the gain in capture rate δ as the relative difference between capture rates by a vibrating and a fixed cylinder

$$\delta = \frac{\langle \eta \rangle - \langle \eta \rangle_{\text{fixed}}}{\langle \eta \rangle_{\text{fixed}}}. \quad (24)$$

As shown in figure 10, the gain is also a bell-shaped function. In table I we give the values of the maximum gain for each Reynolds number. The peak starts from 25% for $Re = 50$, and reaches values 36-40% for $Re = 100, 150$, and 200 .

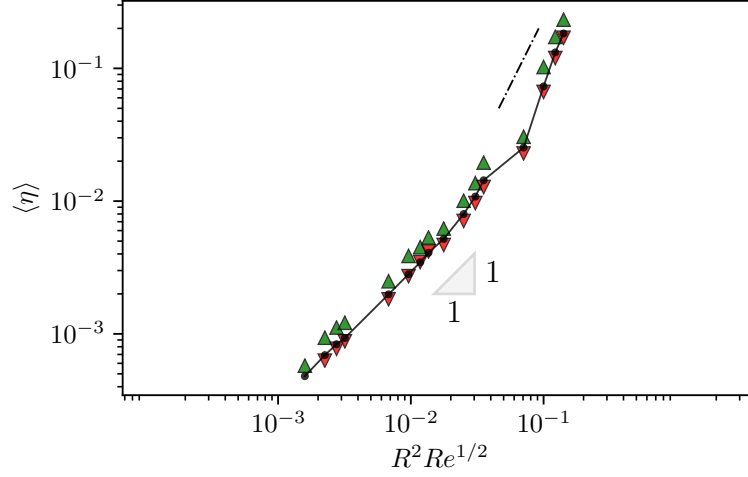


FIG. 9. Mean capture rate of the fixed cylinder (\bullet) and the vibrating cylinder (\blacktriangle , $U_r = 5$ and \blacktriangledown , $U_r = 13$) versus the product $R^2 Re^{1/2}$. For $R^2 Re^{1/2} \lesssim 0.06$ the capture rate varies as $\langle \eta \rangle \sim \langle \eta \rangle_{\text{fixed}} \sim R^2 Re^{1/2}$. Beyond this value, the scaling deviates to $R^2 Re$, as indicated by the dash-dotted line ($- \cdot -$).

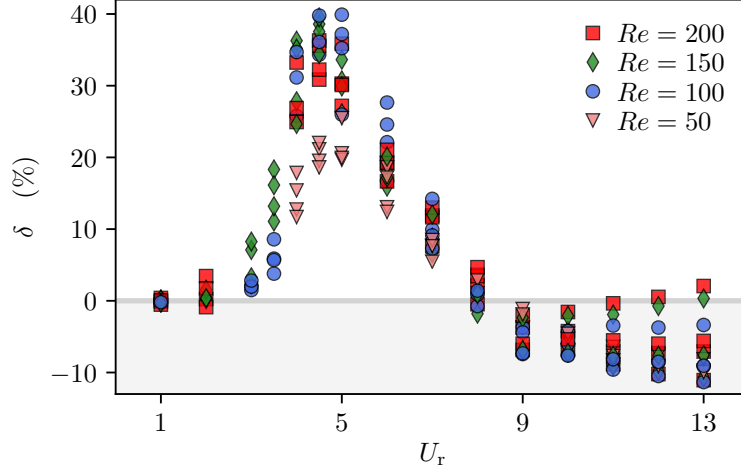


FIG. 10. Variation of the gain in capture rate versus the reduced velocity for all simulation cases $0.015 \leq R \leq 0.1$ and $50 \leq Re \leq 200$.

The cylinder motion has an appreciable effect on particle capture. The resemblance of the curve δ vs. U_r with the curve of lock-in amplitude response [55] warrants a deeper look as a cylinder-dependent variable must intervene in the value of δ . In fact, from a kinematic perspective, the curves of δ have the same profile as the responses of the transverse and stream-wise amplitudes of the cylinder Y_{max} and X_{max} , as shown in figure 11. These amplitudes also start from zero for small reduced velocities, peak at lock-in, then decrease and saturate for large U_r .

In figure 12, the gain δ is plotted against $\bar{Y}_{\text{max}} = Y_{\text{max}}/D$ and $\bar{X}_{\text{max}} = X_{\text{max}}/D$. Beyond certain amplitude thresholds $\bar{Y}_{\text{max}} \gtrsim 0.3$ and $\bar{X}_{\text{max}} \gtrsim 0.01$, δ is an increasing function of the amplitudes. This result is intuitive because the cylinder filters a wider cross-flow space for large \bar{Y}_{max} and encounters more particles. Also, a cylinder with a large \bar{X}_{max} would have more space to accelerate against the stream and reach important counter-current velocities, which

Reynolds number	50	100	150	200
Maximum gain (%)	25.5	39.9	39.5	36.3

TABLE I. The peak value of the gain in capture δ for each Reynolds number Re .

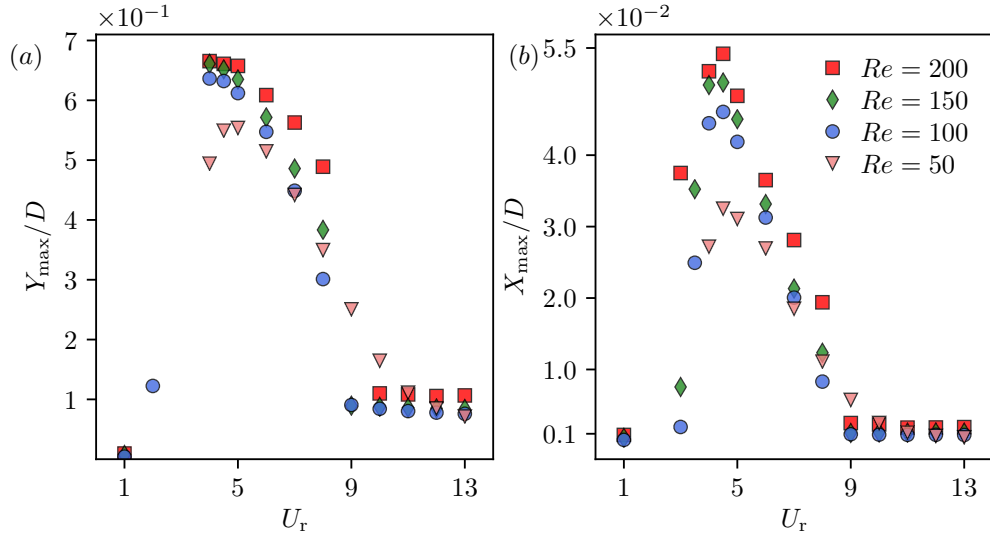


FIG. 11. Numerical response of (a) the transverse and (b) the stream-wise amplitudes of the cylinder.

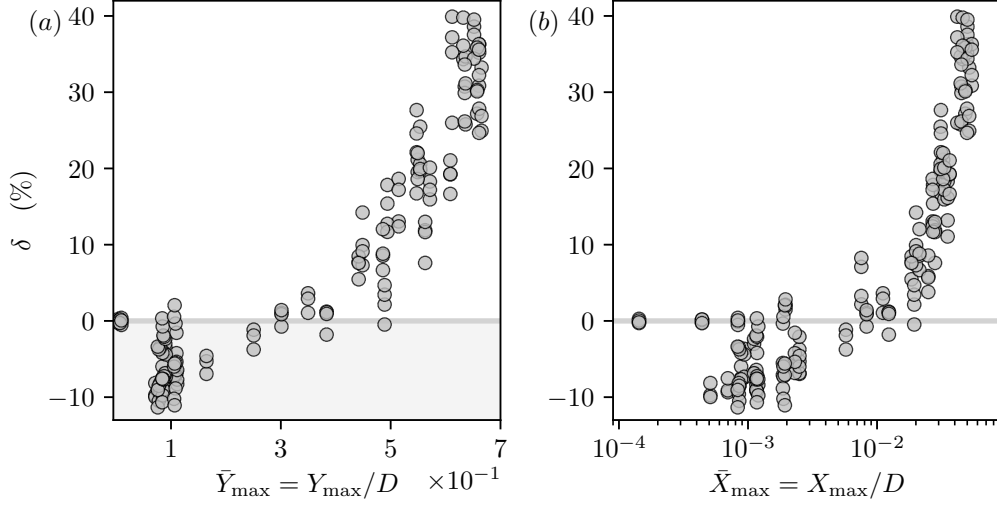


FIG. 12. Variation of the gain in capture rate versus the transverse and stream-wise amplitudes of the cylinder for all simulation cases $0.015 \leq R \leq 0.1$ and $50 \leq Re \leq 200$. The x -axis in (b) is logarithmic to visualise better the staggered data points.

increases the speed of particles relative to the cylinder frame and subsequently the capture rate. For $\bar{Y}_{\max} > 0.2$ and $\bar{X}_{\max} > 0.01$, the results collapse into a single increasing curve (in particular, they vary linearly with \bar{X}_{\max}).

In figure 12, it is worth noting that, past the lock-in peak ($U_r > 9$), the vibration of the cylinder becomes detrimental to capture. This zone corresponds to the amplitudes $0.1 < \bar{Y}_{\max} < 0.3$ and $10^{-3} < \bar{X}_{\max} < 0.01$. In figure 12, this detrimental region has data points of δ that are staggered between -10% and 0% around $\bar{Y}_{\max} = 0.1$ and $\bar{X}_{\max} = 10^{-3}$, instead of a clear monotonic variation. One way to explain this drop in capture is that while U_r increases, the cylinder not only spans short transverse distances, but it also slows down and its period becomes larger than the characteristic time of the particle advection. The particles would then see a cylinder that switches places up and down slowly, staying a long time in either side, hence giving them the opportunity to escape capture. For this reason, the cylinder misses several interception events, so it would be better if it stayed fixed, or at least in a quasi-steady state $U_r \gtrsim 20$ [51]. From this viewpoint, we expect the general profile of the curves $\delta(U_r)$ would have an ascending phase ($0 < U_r < 5$), a peak at lock-in ($U_r \approx 5$), a descending phase ($5 < U_r < 9$), a detrimental regime below zero ($9 < U_r < 20$), and a plateau towards zero beyond the quasi-steady state ($U_r > 20$).

The matching between the gain δ and the amplitudes of the cylinder is emphasised if we consider the *slenderness*

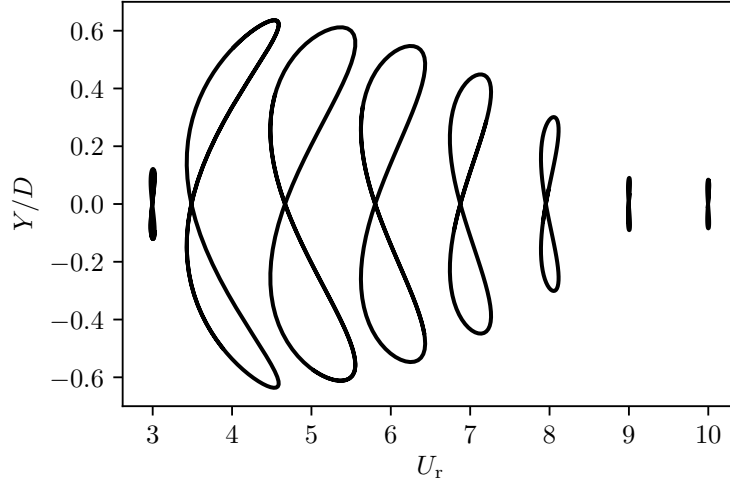


FIG. 13. Shape of the lemniscate limit-cycle trajectory of the cylinder in a flow at $Re = 100$ versus the reduced velocity. The x -span of each lemniscate is magnified about 13 times to elucidate the loops.

ratio of its lemniscate limit-cycle trajectory defined as

$$\gamma = \frac{Y_{\max}}{X_{\max}}. \quad (25)$$

Whereas Y_{\max} and X_{\max} give the dimensions of the lemniscate, γ informs on its slenderness: a small γ illustrates an extended lemniscate, and a large γ illustrates a thin lemniscate. From figure 13 we see that the lemniscate is extended around lock-in $U_r \sim 5$ and thin outside.

Figure 14(b) shows the graph of δ versus γ . We see that there is a critical slenderness $\gamma^* \approx 40$ splitting the domain into extended lemniscates ($\gamma < 40$) and thin lemniscates ($\gamma > 40$). In the region of extended lemniscates, the vibration is beneficial, and the data points collapse well around two branches: a lower branch ($\delta \gtrsim 0$) corresponding to the small reduced velocities, and an upper branch corresponding to lock-in. In the region of thin lemniscates, the vibration is detrimental, and data points scatter. This lack of correlation in the detrimental range is also observed in the response of the slenderness itself, as noticed in figure 14(a). Indeed, while γ preserves the same values irrespective of the Reynolds number in the beneficial range ($1 \leq U_r \leq 8$ and $\gamma < 40$), it either keeps increasing for $Re = 50$ or plateaus towards different values for $100 \leq Re \leq 200$ in the detrimental range ($U_r > 9$ and $\gamma > 40$). Hence, it appears that the response of γ dictates the outcome of vibrations: whenever the slenderness preserves a unique variation irrespective of the Reynolds number, the vibration is beneficial and the gain δ follows a clear trend, otherwise the vibration is detrimental and the variation of the gain δ remains unclear. That is to say, the shape of the lemniscate gives a clue about the impact of vibrations on capture.

VI. BIOLOGICAL INSIGHT

From our simulations, we have seen that a spring-mounted rigid cylinder under VIV can capture up to 40% more particles than its fixed counterpart in an optimal range of reduced velocities, corresponding to the lock-in range $U_r \sim 5$. From a biological point of view, a 40% increase of food availability is significant, however, it occurs over a defined range of flow speeds, cylinder diameters, and cylinder frequencies. The existence of an optimal capture rate implies that the flow and cylinder properties must combine in such a way that U_r remains around the peak and avoids the tails of the bell-shaped curve of δ vs. U_r .

If we consider the more realistic case of an elastic rod subjected to flow, we can expect two sources of additional complexity: a continuous system (i) vibrates with mode shapes and (ii) possesses many natural frequencies. Whereas VIV of the spring-mounted cylinder involve a motion of the entire collector, only a fraction of a continuous system vibrates when it is excited in one mode shape. Then, one could think that a continuous three-dimensional system would limit the gain in capture. But in reality we expect that the curve of the gain in capture $\delta(U_r)$ would comprise several peaks around multiple optimal lock-in regions U_r^{opt} , associated with the natural frequencies of the continuous system. Thus, once δ decreases after the first peak, it shall increase again and reach the following peak, and so forth

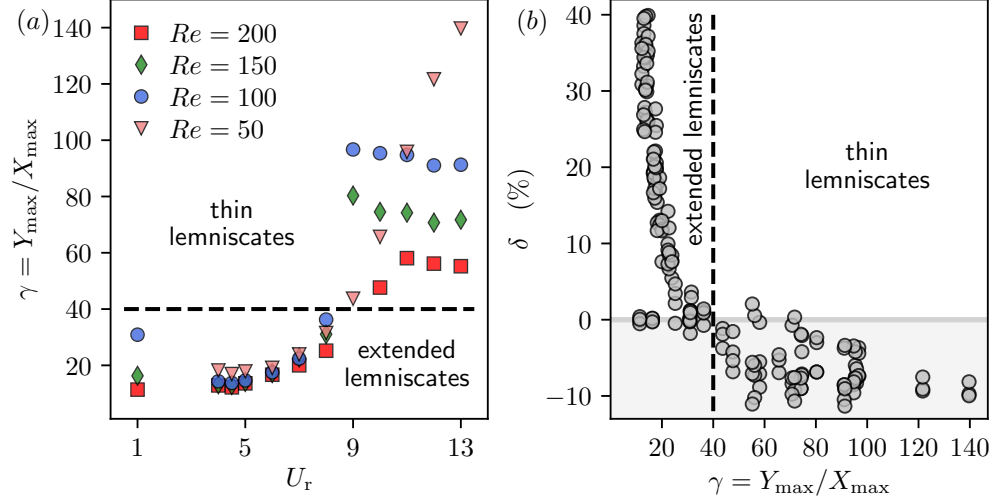


FIG. 14. (a) Slenderness ratio of the lemniscate limit-cycle trajectory of the cylinder versus the reduced velocity for the Reynolds numbers $50 \leq Re \leq 200$. For low reduced velocities, γ starts from a relatively small value, and decreases until reaching the minimum at lock-in ($U_r \approx 5$). From $U_r = 1$ to 8, the slenderness ratio for all Reynolds numbers follow the same trend. Beyond $U_r = 8$, it keeps increasing for $Re = 50$, while it plateaus for $100 \leq Re \leq 200$. (b) Gain in capture rate versus the slenderness ratio of the lemniscate for all simulation cases $0.015 \leq R \leq 0.1$ and $50 \leq Re \leq 200$. For $\gamma < 40$, data points converge around two branches. The lower branch, which is close to the zero value, corresponds to low reduced velocities, whereas the upper branch represents the region around lock-in. The dashed line in both graphics is the critical value $\gamma^* = 40$ cutting the domain in two regions: extended lemniscates for $\gamma < 40$ and thin lemniscates for $\gamma > 40$.

for each U_r^{opt} without finding a gap to drop below zero. We deduce that having multiple natural frequencies ensures that a soft coral colony can achieve lock-in in varying environments.

These continuous system considerations imply that soft corals could benefit from tuning their morphology (e.g. length and diameter of branches, size of polyps) as well as their structural properties (e.g. flexural rigidity of the skeleton) according to the typical ambient water speed. They could tune their properties in order to match one of the optimal reduced velocities U_r^{opt} , trigger VIV, and achieve the best feeding rate.

Let us assimilate the soft coral branch to an elastic rod having a diameter D , length L , mass per unit length m_1 (including the added mass), and flexural rigidity EI . The reduced velocity reads

$$U_r = St \frac{U_0}{D} \sqrt{\frac{m_1 L^4}{EI}}, \quad (26)$$

where St is the Strouhal number. Here U_r equals the ratio of the vortex shedding frequency StU_0/D to the characteristic frequency of the structure $\sqrt{EI/m_1 L^4}$. Considering that $I \sim D^4$ and writing $m_1 \sim \rho D^2$, we see that a reduced velocity sticking around the optimal range should verify

$$StU_0 \left(\frac{\rho}{E} \right)^{1/2} \frac{L^2}{D^2} \sim U_r^{\text{opt}} (= \text{const}). \quad (27)$$

Introducing the aspect ratio $\Gamma = L/D$ and the speed (of sound) $c_s = \sqrt{E/\rho}$, equation (27) is equivalent to

$$\frac{c_s}{\Gamma^2} \propto U_0. \quad (28)$$

Relation (28) connects the morphological properties of the soft coral (Γ and c_s) on the left-hand side with the ambient water speed (U_0) on the right-hand side. It led us to ask the following question: if the soft coral happens to tune its morphology to cope with the local predominant currents, which property should it choose to tune? A simple reasoning based on the relation (28) reveals that in deep waters where the flow is globally calm (small U_0), soft corals would need thin branches (slender phenotype, large Γ) and a soft skeleton (small c_s). Conversely, in shallow waters where the flow is turbid (high U_0), they would need thick branches (stout, bushy phenotype, small Γ) and a stiff skeleton (large c_s). Physiological compromise should limit the extreme values of c_s/Γ^2 . A soft coral with both thin branches and soft skeleton would be too flimsy and pushed down by the flow, making it unable to filter or capture any particle.

It would also put it at risk of predators. Conversely a soft coral with both thick and stiff branches would require too much energy to maintain a proper metabolism and large strain to flex.

Jeyasuria and Lewis [7] measured the Young's modulus of the skeleton for several soft corals, and found that deep-water species are stiffer than shallow-water ones. Moreover, the morphological comparison between bipinnate sea plumes in different habitats carried out by Sánchez *et al.* [8] indicates that deep-water corals have larger aspect ratios than their shallow-water counterparts. Considering these ecological observations, we conjecture that tuning the aspect ratio Γ is the solution that soft corals prefer in order to maximise particle interception. This fact can also be intuitively inferred if we notice that the aspect ratio is squared in equation (28).

VII. CONCLUSION AND FUTURE WORK

In this paper, we inquire about the observed high frequency vibrations of the branches of the soft coral *A. bipinnata*. First we diagnose the origin of vibration. From numerical and qualitative arguments, we find that VIV are the most plausible cause of these fast dynamics. Then we investigate the rate of particle interception. We model the coral branch as a cylinder of circular cross-section. Instead of imposing a vibration amplitude or frequency, we let it free to oscillate under VIV in both transverse and stream-wise directions. Besides, we assimilate food particles to spheres and subject them to drag, pressure load, and added mass force. The simulation of their trajectories and the calculation of the capture rate show that the vibrating cylinder, at lock-in, can intercept up to 40% more particles than a fixed cylinder. These simulations also reveal, conversely, the existence of a range of reduced velocities after lock-in where the vibrations are detrimental for capture. For this reason, we cautiously avoid affirming that vibrations are either totally beneficial or totally detrimental, and bring back the evaluation of the interception efficiency by referring to the regime of reduced velocities instead.

In the present simulations we vary the Reynolds numbers and particle sizes. Though, on the one hand, we consider a constant mass ratio of the cylinder $M = 1$ and neglect structural damping $\zeta = 0$. Because increasing the product $M\zeta$ shortens the amplitude of vibration Y_{\max} [78], we expect from the function $\delta(Y_{\max})$ in figure 11(a) that the cylinder would lose in particle capture. On the other hand, we consider particles having the same density ratio, twice heavier than water $\bar{\rho} = 2$. For a given Reynolds number, the particle density affects the capture efficiency depending on its size. Espinosa-Gayosso *et al.* [65] showed, for $Re \sim 100$, that a weakly buoyant particle slightly lighter than water ($\bar{\rho} = 0.9$) would never beat the efficiency scored by a heavy sediment-type particle ($\bar{\rho} = 2.6$) if it is big. They also showed, conversely, that the discrepancy between a weakly buoyant particle and a sediment-type one disappears as long as the particle is small. It would be enriching to carry out a parametric study, and highlight the dependency of the capture efficiency on the density between these two extremes.

In addition, our model of particle advection is more appropriate for passive particles. In reality, some particles are motile and might dodge and escape capture. Although their propulsion force turns helpless when the water current is important, it is worth taking it into account and determine the flow regimes where the motility influences the capture. Furthermore, instead of the solid contact criterion, a more realistic capture condition may consider some capture zones around polyps, with areas representing tentacles reach, and each of them having a probability of successful catch. Another improvement of the capture criterion might be to assign a retention duration to particles directly hitting the cylinder edge, in order to reflect the retaining action of the mucus.

To launch avenues with invertebrate biology, we encourage taking over our insight in section VI by conducting *in situ* experiments on *A. bipinnata* and other soft corals, in order to get their mechanical characteristics and study their dynamical behaviour. Another helpful set of experiments to understand biological plasticity would be to transplant soft corals in different habitats and investigate how their natural frequencies and modes in water vary.

In the end, it is worth reflecting on how a flow-induced instability can be turned into a strategy. At a time when VIV represent a major threat to offshore energy production, the soft coral paradigm unveils an advantageous side of this instability that can spark novel ideas in biomimetics. Soft corals may, for instance, bioinspire engineers to design innovative energy harvesters at sea, and seek – instead of suppress – VIV as a principal supplier to harness clean and renewable energy.

Supplementary data. Dynamical equations and numerical methods used in the elastic rod simulations in section II, as well as a verification of the particle advection code in section III, are available at <https://doi.org/10.xxxx/jfm.2021...>

Acknowledgements. We would like to thank Camille Soenen for performing measurements on living soft corals and extracting their mechanical properties.

Funding. The authors acknowledge the financial support from Discovery Grants Nos. RGPIN-2019-07072, RGPIN-2019-05335, as well as from the Simulation-Based Engineering Science (SBES) program through the CREATE grant

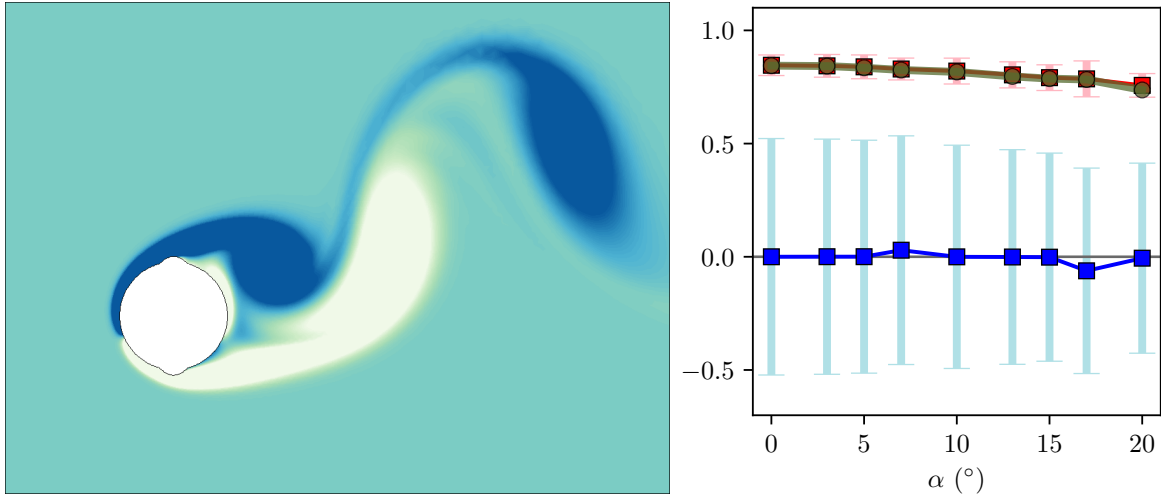


FIG. 15. Left: vorticity contour plot of a flow around an idealised soft coral cross-section at the angle of attack 20° and Reynolds number $Re = 200$. The cross-section is a circle, and polyps are the two diametrically opposed arcs of circle. Their size is 10% of the circle diameter. Right: mean values of the fluctuating drag and lift coefficients, C_D (■) and C_L (■). The bars refer to the maximum and minimum values of the variables. The mean value of $dC_L/d\alpha + C_D$ (●) is calculated from cubic spline interpolation of data points.

of the National Science and Engineering Research Council of Canada (NSERC).

Declaration of Interests. The authors report no conflict of interest.

Author ORCID. M. Boudina, <https://orcid.org/0000-0002-4908-4589>; F. P. Gosselin, <https://orcid.org/0000-0003-0639-7419>; S. Étienne, <https://orcid.org/0000-0003-2813-0061>.

Appendix A: Refuting galloping as a cause of soft coral vibrations

The dried bipinnate sea plume in figure 3 have protuberances along its branches, then are not perfect circular cylinders. To see whether this geometrical perturbation is small enough to leave the branch safe from galloping, we considered an idealised cross-section of *A. bipinnata* as shown in figure 15, left. We modelled protuberances as diametrically opposed arcs of circle having a size of 10% of the cylinder diameter, in order to conform to the photography in figure 3 and data provided by Bayer [44]. We simulated flows of different angles of attack α around this geometry using the same in-house flow solver [56] described in section III A, then evaluated the Glauert-den Hartog criterion. This latter states that a sufficient condition for galloping to arise is

$$\frac{dC_L}{d\alpha} + C_D < 0, \quad (\text{A1})$$

where C_L and C_D are the lift and drag coefficients. From the video of the vibrating coral we estimated that the transverse displacement of the branch does not exceed $Y_{\max}/D \sim 0.5$. The angle of attack to which the coral cross-section would be exposed is then at most $\tan^{-1}(2\pi f_n A/U_0) \sim 24^\circ$. Therefore, we chose a representative range of α between 0° and 20° . Figure 15, right, shows the variation of the fluid-dynamic coefficients and the Glauert-den Hartog criterion. The quantity $dC_L/d\alpha + C_D$ is always close to 1 and has no tendency to change sign in the range of α considered, ensuring that galloping cannot be a cause of the high frequency motion of the soft coral branches.

-
- [1] M. Ribes, R. Coma, and J.-M. Gili, *Limnology and Oceanography* **43**, 1170 (1998), publisher: John Wiley & Sons, Ltd.
 - [2] S. A. Wainwright and J. R. Dillon, *Biol Bull* **136** (1969), 10.2307/1539674.
 - [3] G. C. Williams and J.-Y. Chen, *Zootaxa* **3505**, 39 (2012).
 - [4] F. P. Gosselin, *Journal of Experimental Botany* **70**, 3533 (2019).

- [5] S. Vogel, *American Zoologist* **24**, 37 (1984).
- [6] E. de Langre, *Annual Review of Fluid Mechanics* **40**, 141 (2008).
- [7] P. Jeyasuria and J. Lewis, *Coral reefs* **5**, 213 (1987).
- [8] J. A. Sánchez, C. Aguilar, D. Dorado, and N. Manrique, *BMC Evolutionary Biology* **7**, 122 (2007).
- [9] T. Leclercq and E. de Langre, *Journal of Fluid Mechanics* **838**, 606 (2018).
- [10] J. Lei and H. Nepf, *Journal of Fluids and Structures* **87**, 137 (2019).
- [11] M. Rodriguez, E. de Langre, and B. Moulia, *American Journal of Botany* **95**, 1523 (2008).
- [12] M. Rodriguez, S. Ploquin, B. Moulia, and E. de Langre, *Journal of Applied Mechanics* **79**, 044505 (2012).
- [13] C. Der Loughian, L. Tadriss, J.-M. Allain, J. Diener, B. Moulia, and E. de Langre, *Comptes Rendus Mécanique* **342**, 1 (2014).
- [14] C. Williamson and R. Govardhan, *Annual Review of Fluid Mechanics* **36**, 413 (2004).
- [15] T. Sarpkaya, *Wave Forces on Offshore Structures* (Cambridge University Press, 2010).
- [16] J. Fredsøe and M. B. Sumer, *Hydrodynamics Around Cylindrical Structures (Revised Edition)* (World Scientific, 2006).
- [17] S. Etienne and D. Pelletier, *Journal of Fluids and Structures* **31**, 18 (2012).
- [18] R. E. D. Bishop and A. Y. Hassan, *Proc. R. Soc. Lond. A* **277**, 51 (1964).
- [19] J. R. Chaplin, P. W. Bearman, F. J. Huera Huarte, and R. J. Pattenden, *Journal of Fluids and Structures Fluid-Structure and Flow-Acoustic Interactions Involving Bluff Bodies*, **21**, 3 (2005).
- [20] D. J. Newman and G. E. Karniadakis, *Journal of Fluid Mechanics* **344**, 95 (1997).
- [21] M. L. Facchinetti, E. de Langre, and F. Biolley, *European Journal of Mechanics - B/Fluids Bluff Body Wakes and Vortex-Induced Vibrations*, **23**, 199 (2004).
- [22] C. Evangelinos and G. E. Karniadakis, *Journal of Fluid Mechanics* **400**, 91 (1999), publisher: Cambridge University Press.
- [23] D. Lucor, H. Mukundan, and M. S. Triantafyllou, *Journal of Fluids and Structures "Bluff Body Wakes and Vortex-Induced Vibrations (BBVIV-4)"*, **22**, 905 (2006).
- [24] R. Violette, E. de Langre, and J. Szydlowski, *Computers & Structures Fourth MIT Conference on Computational Fluid and Solid Mechanics*, **85**, 1134 (2007).
- [25] S. Kim, H. Park, H. A. Gruszecki, D. G. Schmale, and S. Jung, *Proceedings of the National Academy of Sciences* **116**, 4917 (2019), publisher: National Academy of Sciences Section: Biological Sciences.
- [26] M. M. Chance and D. A. Craig, *Canadian Journal of Zoology* **64**, 1295 (1986), publisher: NRC Research Press.
- [27] L.-E. Widahl, *Annals of the Entomological Society of America* **85**, 91 (1992), publisher: Oxford Academic.
- [28] K. E. Fabricius, in *Encyclopedia of Modern Coral Reefs* (Springer Science & Business Media, 2011) pp. 740–745.
- [29] J. E. N. Veron, in *Encyclopedia of Modern Coral Reefs* (Springer Science & Business Media, 2011) pp. 275–281.
- [30] J. Shimeta and M. A. R. Koehl, *Journal of Experimental Marine Biology and Ecology* **209**, 47 (1997).
- [31] M. E. Weber and D. Paddock, *Journal of Colloid and Interface Science* **94**, 328 (1983).
- [32] M. R. Palmer, H. M. Nepf, T. J. R. Pettersson, and J. D. Ackerman, *Limnology and Oceanography* **49**, 76 (2004).
- [33] N. E. L. Haugen and S. Kragset, *Journal of Fluid Mechanics* **661**, 239 (2010).
- [34] A. Espinosa-Gayosso, M. Ghisalberti, G. N. Ivey, and N. L. Jones, *Journal of Fluid Mechanics* **710**, 362 (2012).
- [35] A. Espinosa-Gayosso, M. Ghisalberti, G. N. Ivey, and N. L. Jones, *Journal of Fluid Mechanics* **733**, 171 (2013).
- [36] J. Krick and J. D. Ackerman, *Journal of Theoretical Biology* **368**, 13 (2015).
- [37] D. McCombe and J. D. Ackerman, *The American Naturalist* **192**, 81 (2018).
- [38] K. J. Niklas, *The Botanical Review* **81**, 28 (2015).
- [39] S. Inoue, H. Kayanne, S. Yamamoto, and H. Kurihara, *Nature Climate Change* **3**, 683 (2013).
- [40] G. Tsounis and P. J. Edmunds, *Ecosphere* **8**, e01646 (2017).
- [41] S. G. Monismith, *Annual Review of Fluid Mechanics* **39**, 37 (2007).
- [42] YouTube, "Caribbean Spiny Lobster and a Bipinnate Sea Plume coral," (2013), <https://youtu.be/1mgAyFgYfYw>.
- [43] J. Schindelin, I. Arganda-Carreras, E. Frise, V. Kaynig, M. Longair, T. Pietzsch, S. Preibisch, C. Rueden, S. Saalfeld, B. Schmid, J.-Y. Tinevez, D. J. White, V. Hartenstein, K. Eliceiri, P. Tomancak, and A. Cardona, *Nature Methods* **9**, 676 (2012).
- [44] F. M. Bayer, *Studies on the Fauna of Curaçao and other Caribbean Islands* **12**, 1 (1961).
- [45] S. D. Cairns, *Gulf and Caribbean Research* **6**, 9 (1977).
- [46] RodiCS, "RodiCS: a finite element solver of kirchhoff rods under fluid flow and more," (2020), <https://zenodo.org/record/4023287>.
- [47] M. Alnæs, J. Blechta, J. Hake, A. Johansson, B. Kehlet, A. Logg, C. Richardson, J. Ring, M. E. Rognes, and G. N. Wells, *Archive of Numerical Software* **3** (2015), 10.11588/ans.2015.100.20553, number: 100.
- [48] G. I. Taylor, *Proceedings of the Royal Society of London. Series A. Mathematical and Physical Sciences* **214**, 158 (1952), publisher: Royal Society.
- [49] M. L. Facchinetti, E. de Langre, and F. Biolley, *Journal of Fluids and Structures* **19**, 123 (2004).
- [50] NDBC, "<https://www.ndbc.noaa.gov/>," (2020).
- [51] R. Blevins, *Flow-induced vibration* (Van Nostrand Reinhold, 1990).
- [52] F. J. Huera-Huarte and M. Gharib, *Journal of Fluids and Structures* **27**, 354 (2011).
- [53] Nova South Eastern University, "South Florida Octocorals: A Guide to Identification," (2016).
- [54] Y. Nakamura, K. Hirata, and K. Kashima, *Journal of Fluids and Structures* **8**, 355 (1994).
- [55] M. Paidoussis, S. Price, and E. de Langre, *Fluid-Structure Interactions: Cross-Flow-Induced Instabilities* (Cambridge University Press, 2010).
- [56] S. Etienne, A. Garon, and D. Pelletier, *Journal of Computational Physics* **228**, 2313 (2009).

- [57] H. Persillon and M. Braza, *Journal of Fluid Mechanics* **365**, 23 (1998).
- [58] C. Taylor and P. Hood, *Computers & Fluids* **1**, 73 (1973).
- [59] M. R. Maxey and J. J. Riley, *The Physics of Fluids* **26**, 883 (1983).
- [60] H. Ounis and G. Ahmadi, *Journal of Fluids Engineering* **112**, 114 (1990).
- [61] I. E. Barton, *Journal of Aerosol Science* **26**, 887 (1995).
- [62] R. Clift, J. R. Grace, and M. E. Weber, New York **510**, 147 (1978).
- [63] C. E. Brennen, *A Review of Added Mass and Fluid Inertial Forces.*, Tech. Rep. (Naval Civil Engineering Laboratory, Port Hueneme, California, 1982).
- [64] C. Béguin, E. Pelletier, and S. Étienne, *European Journal of Mechanics - B/Fluids* **56**, 28 (2016).
- [65] A. Espinosa-Gayosso, M. Ghisalberti, G. N. Ivey, and N. L. Jones, *Journal of Fluid Mechanics* **783**, 191 (2015).
- [66] A. Hay, K. R. Yu, S. Etienne, A. Garon, and D. Pelletier, *Computers & Fluids* **100**, 204 (2014).
- [67] K. R. Yu, S. Étienne, A. Hay, and D. Pelletier, *Theoretical and Computational Fluid Dynamics* **29**, 455 (2015).
- [68] J.-F. Cori, S. Etienne, A. Garon, and D. Pelletier, *International Journal for Numerical Methods in Fluids* **78**, 385 (2015).
- [69] A. Hay, S. Etienne, A. Garon, and D. Pelletier, *Computer Methods in Applied Mechanics and Engineering* **295**, 172 (2015).
- [70] K. R. Yu, S. Étienne, Y.-M. Scolan, A. Hay, E. Fontaine, and D. Pelletier, *Journal of Fluids and Structures* **60**, 37 (2016).
- [71] A. Hay, S. Etienne, D. Pelletier, and A. Garon, *Journal of Computational Physics* **291**, 151 (2015).
- [72] PARADVECT, “PARADVECT (PARTicle ADVECTION): a Python code to simulate the trajectory of particles advected by a fluid flow,” (2020).
- [73] R. Löhner and J. Ambrosiano, *Journal of Computational Physics* **91**, 22 (1990).
- [74] R. Löhner, *Applied Computational Fluid Dynamics Techniques: An Introduction Based on Finite Element Methods* (John Wiley & Sons, 2008).
- [75] E. Buckingham, *Physical Review* **4**, 345 (1914), publisher: American Physical Society.
- [76] J. Shimeta and P. A. Jumars, *Oceanogr. Mar. Biol. Annu. Rev* **29**, 1 (1991).
- [77] M. Boudina, F. P. Gosselin, and S. Étienne, *Physics of Fluids* **32**, 123603 (2020).
- [78] A. Khalak and C. H. K. Williamson, *Journal of Fluids and Structures* **13**, 813 (1999).